## Author Statement:

**Aqeel Al-Hamaidah:** Methodology, Formal analysis, Investigating, Writing-Original draft

**Mahmood Rezaee Roknabadi:** Term, Conceptualization, Resources, Writing-Review&Editing

**Malek Bagheri Harouni:** Supervision, Resources, Writing-Review&Editing, Funding acquisition

**Bizhan Malaekeh-Nikouei:** Validation, Resources, Writing-Review&Editing

**Asma Mahmoudi:** Validation, Resources

**Reza Ghanbari:** Visualization, Writing-Review&Editing

**Alireza Charmforoushan:** Methodology, Writing-Original draft

# Synthesis of Multifunctional Superparamagnetic Mesoporous $ZnMnFe_2O_4$@Fe-$CaSiO_3$ Core-shell for Medical Applications

*Aqeel Al-Hamaidah[1],Mahmood Rezaee Roknabadi[2,3],Malek Bagheri Harouni[1], Bizhan Malaekeh-Nikouei[4,5], Asma Mahmoudi[6], Reza Ghanbari[2], Alireza Charmforoushan[3,7]*

*[1]Department of Physics, Faculty of Science, University of Isfahan, Isfahan, Iran*

*[2]Department of Physics, Faculty of Science, Ferdowsi University of Mashhad, Mashhad, Iran*

*[3]Ångstrom Thin Film Research Laboratory, Faculty of Science, Ferdowsi University of Mashhad, Mashhad, Iran*

*[4]Nanotechnology Research Center, Pharmaceutical Technology Institute, Mashhad University of Medical Sciences, Mashhad, Iran*

*[5]Department of Pharmaceutics, School of Pharmacy, Mashhad University of Medical Sciences, Mashhad, Iran*

*[6] Department of Pharmaceutical Nanotechnology, School of Pharmacy, Mashhad University of Medical Sciences, Mashhad, Iran*

*[7]Aerosol Physics Laboratory, Physics Unit, Faculty of Engineering and Natural Sciences, Tampere University, Tampere, Finland*

## Abstract

Herein, we report the synthesis of a mesoporous calcium silicate superparamagnetic nanoparticle as $ZnMnFe_2O_4$@Fe-$CaSiO_3$ core-shell. This core-shell nanocomposite reveals excellent properties such as mesoporous nanocomposite, superparamagnetic at room temperature, low toxicity, large surface area, tunable pore size, and easy surface manipulation. The core nanocomposite ($ZnMnFe_2O_4$) is synthesized by the hydrothermal method, which shows a superparamagnetic behavior with an excellent saturation magnetization of 52.09 emu/g. The core-shell structure is prepared by a micellar-assisted sol-gel method, which uses a copolymer to create pores in the structure of $CaSiO_3$. To improve the magnetic properties of the core-shell structure, different percent of Fe ions (0%, 5%, and 10%) are doped onto the calcium silicate structure; as for 10% Fe, i.e., $ZnMnFe_2O_4$@Fe10-$CaSiO_3$, saturation magnetization and coercive magnetic field are 34.543 emu/g and 1Oe, respectively. In this configuration of nanocomposite, the pore volume and superparamagnetic property increase simultaneously. In addition, the core-shell mesoporous $ZnMnFe_2O_4$@Fe-$CaSiO_3$ nanocomposite reveals comparable mesoporous channels (3.4–6 nm), while the amorphous structure of $CaSiO_3$ has not been changed. These core-shell mesoporous superparamagnetic nanocomposites are evaluated in terms of drug loading and release using

epirubicin (EPI) as a model drug. It is found that the increase of iron ions improves the capacity to stabilize the pH environment. Additionally, the mesoporous Fe-$CaSiO_3$ nanostructures demonstrate a sustained drug release property that could be useed in local drug delivery therapy. Therefore, these mesoporous superparamagnetic nanostructures would be a promising multifunctional platform for local drug delivery, magnetic resonance imaging, magnetic hyperthermia, and bone tissue regeneration.

**Keywords:** core-shell nanoparticles; superparamagnetic; mesoporous; epirubicin (EPI); drug delivery

## 1- Introduction

Nowadays, the targeted delivery of drugs is highly regarded as a successful and important method in the treatment of certain diseases. Targeted drug delivery involves specifically carrying and releasing the drug into the tumor area or damaged tissues and reducing drug leakage into other healthy tissues or cells. This method not only reduces adverse effects but also improves therapeutic effectiveness and decreases treatment costs compared to the conventional methods [1-3]. In drug targeting, drug molecules accumulate in a target organ or tissue selectively such that the drug concentration at the disease site is high while its concentration in non-targeted organs and tissues is low (preferably below a specific threshold level to prevent any adverse effects) [4, 5]. An ideal target should be druggable, meaning effective, safe, and meeting clinical and commercial requirements [6].

Superparamagnetic nanoparticles are one of the most important substances that can be used in targeted drug delivery systems due to their ability to control drug delivery and release by an applied magnetic field [7, 8]. Besides, they have demonstrated significant potential applications in biomolecule separation [9], as a contrast agent in magnetic resonance imaging (MRI) [10, 11], and, most notably, in hyperthermia cancer therapy [8, 12]. Although their bioproperties are limited, the main disadvantage of these magnetic carriers is their limited drug loading capacity because of their small specific surface area [13]. Different biomaterials, such as organic (polymers) and inorganic (silica, calcium silicate) materials, can cover superparamagnetic nanoparticles to create a solution for the aforementioned issues [14-16].

Wollastonite (WS), which is a calcium silicate mineral ($CaSiO_3$), has been considered a potential candidate for dental roots, drug delivery, and bone tissue engineering due to its excellent biocompatibility, biodegradability, and bioactivity [17, 18]. Furthermore, literature reports have revealed that WS nanoparticles loaded with ibuprofen [19, 20], an anti-cancer docetaxel (DTX) drug [21], or proteins [22] can show a sustained, slow, and controllable release behavior without any surface modification with organic functional groups. Furthermore, micro-mesoporous WS nanoparticles were loaded with a relatively high amount of epirubicin (EPI), and its release behavior investigation revealed a sustained, slow, and pH-responsive release (described in our previous work) [23]. Wu et al. [24] demonstrated that mesoporous WS can load an extremely high amount of ibuprofen (2.29 g/g (drug/carrier)), owing to the chemical nature and porous structure

of WS. Therefore, porous WS nanoparticles are promising for their application in various drug delivery systems with controlled release. Besides, it is well acknowledged that WS has shown excellent bioactivity and biocompatibility in comparison with other inorganic biomaterials (such as silica) and are able to transform into bone-like apatite or hydroxyapatite in phosphate buffered saline or simulated body fluid [25]. Hence, it is suitable for bone-implantable drug delivery applications too.

Mesoporous core-shell magnetic iron oxide-WS nanoparticles were synthesized by B.-Q. Lu et al. [26]. The in-vitro cytotoxicity tests of the DTX-loaded core-shell magnetic Iron Oxide-WS have revealed that the synthesized nanoparticles have the ideal anti-cancer ability. However, saturation magnetization of the core-shell nano carriers was only 6.2 emu/g [26]. Basically, the magnetic properties of nanoparticles are reduced by covering them in the core-shell configuration [27]. To address this issue, a suitable magnetic nanoparticle (for example, iron) can be doped into the WS shell structure. Iron is found in red blood cells and plays a crucial role in the functioning of the human body [28]. Moreover, magnetic mesoporous Fe–$CaSiO_3$ materials could generate heat in an alternating magnetic field for potential application in hyperthermia treatment to treat bone defects caused by bone tumors [29]. Zhang et al. synthesized magnetic mesoporous Fe–$CaSiO_3$ nanoparticles [29]. Then, they showed that the magnetization of the nanoparticles increased with the level of Fe substation in the structure and it had not shown any cytotoxic effects on MC3T3-E1 cells [30].

In the present work, superparamagnetic $Zn_{0.4}Mn_{0.6}Fe_2O_4$ (ZMFO) nanoparticles were successfully synthesized by the hydrothermal method. Then, the nanoparticles were coated with calcium silica by the sol-gel method. Fe ions (0%, 5%, and 10%) were doped onto the calcium silicate structure, P123 was used as the template for the porous structure, and iron was added. The XRD pattern has confirmed the formation of a magnetite phase and an amorphous silica structure. Also, the results of FTIR and TEM analysis show that the coating of nanoparticles (ZMFO) by Fe-$CaSiO_3$ has been done well. BET analysis and nitrogen gas absorption have shown that the synthesized nanocomposites have a mesoporous structure with a high specific surface area of 34.543 $m^2/g$ and a high pore volume of 0.204 $cm^3/g$ for 10% Fe in shell sample ($ZnMnFe_2O_4$@10%Fe-$CaSiO_3$). VSM analysis has confirmed the superparamagnetic property of nanoparticles with a high $M_S$ of 37.22 emu/g and a low $H_C$ of 1 Oe. These high specific surface

area and pore volume, and high $M_S$ and low $H_C$ of the sample cause these composites suitable for targeted drug delivery and biosensor applications. In this configuration of nanocomposite, the pore volume and superparamagnetic property are increased simultaneously. A comparison of the drug release of epirubicin (EPI) at pH 5.5 and 7.2 has shown that drug release occurs faster at pH 5.5, which is similar to cancer cells in the human body.

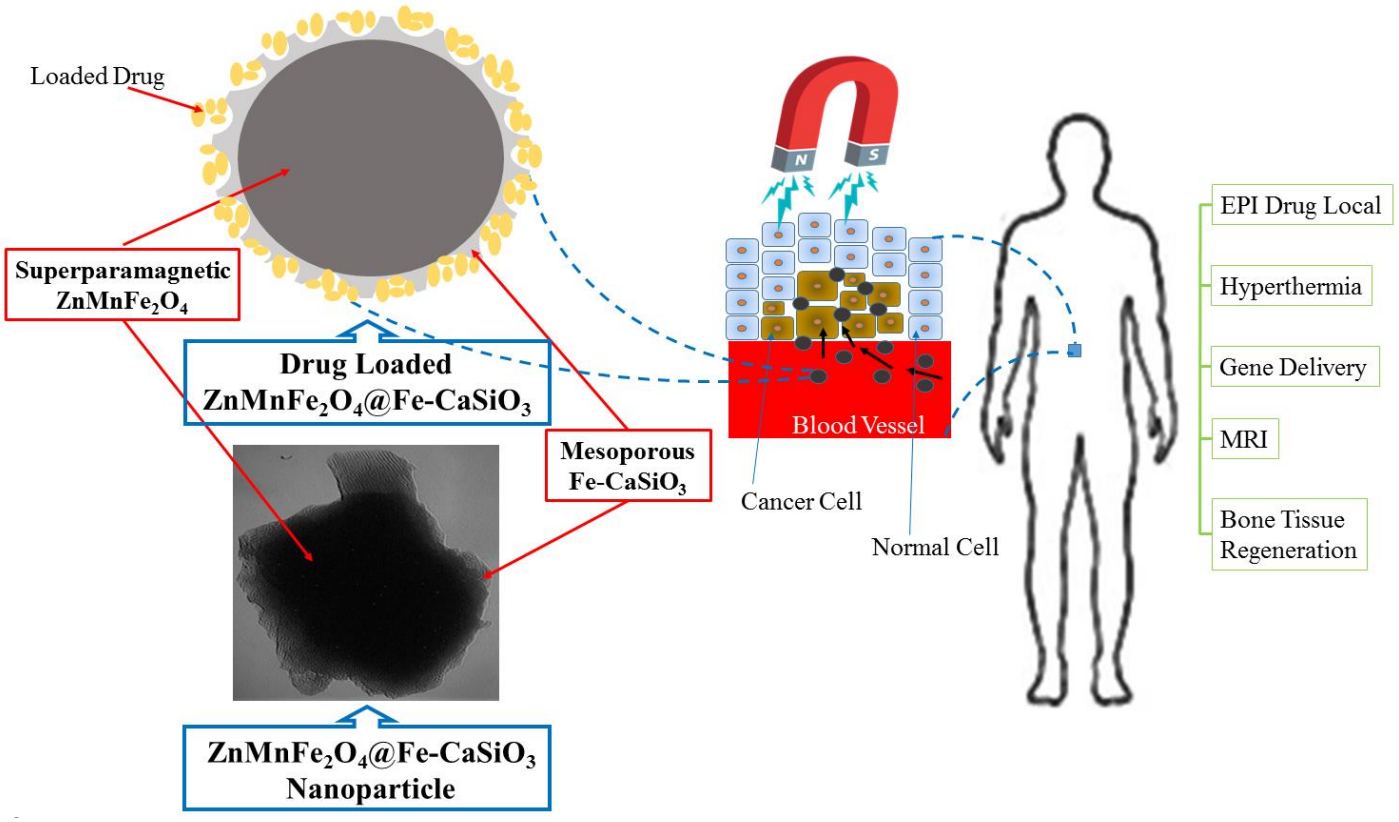


Schem. 1. The schematic illustration of $ZnMnFe_2O_4$@Fe-$CaSiO_3$ nanoparticle and its applications in medical.

## 2- Experimental

### Materials:

Zinc nitrate hexahydrate ($Zn(NO_3)_2.\ 6H_2O$), manganese nitrate hexahydrate ($Mn(NO_3)_2.\ 6H_2O$), ferric nitrate nonahydrate ($Fe(NO_3)_3.\ 9H_2O$), calcium nitrate tetrahydrate ($Ca(NO_3)_2.\ 4H_2O$), Merck), and TEOS $(C_2H_5O)_4Si$ were used as raw materials. Besides, PEG-PPG-PEG

triblock copolymer (P.123, EO20-PO70-EO20, Sigma-Aldrich) was used as the template for porous structure. Feridex was the supplier to MEENA Pharmaceutical.

**Synthesis of $Zn_{0.4}Mn_{0.6}Fe_2O_4$:**

First, 8.2550 g of iron nitrate was dissolved in 20 mL of deionized water and heated to a temperature of 37 °C for 30 min. Then, 1.2575 g of manganese nitrate and 1.5023 g of zinc nitrate were dissolved in 5 mL of deionized water separately. After that, the solutions were mixed together and stirred for 30 min. Then, 0.404 g of sodium hydroxide were dissolved in 10 mL of deionized water, and then, was added drop by drop to the mixture for 15 min, and was magnetically stirred for 30 min at 500 rpm. Then, the mixture was placed in an ultrasonic bath for 10 min. After that, the mixture was transferred into a 200 mL autoclave and heated at 200 °C for 5 h. After cooling, the solid material was washed with ethanol and deionized water several times. Finally, the solid material was dried at 120 °C for 12 h.

**Synthesis $Zn_{0.4}Mn_{0.6}Fe_2O_4$@Fe-$CaSiO_3$:**

$Zn_{0.4}Mn_{0.6}Fe_2O_4$@$CaSiO_3$ nanoparticles were synthesized by a micellar-assisted sol-gel method [29]. As a brief summary, 3 g of P123 was mixed with 20.5 mL of HCl and 130 mL of distilled water at a temperature of 40 °C until the mixture became clear. After that, first 0.1 g of ZMFO nanoparticles were added, and then, 9.64 g of $Ca(NO_3)_2$. 4 $H_2O$, and 8.5 mL of TEOS were added to the mixture. Then, the different percent iron ions (0, 0.82, and 1.65 g) were substituted into the shell structure to improve the magnetic properties of the samples at values of 0%, 5%, and 10% wt rather than Ca. The mixture was kept under constant stirring for 24 h, and then washed with distilled water three times. The precipitate was dried for 12 h at 110 °C. Finally, the as-prepared powder was calcined in air for 3 h at a heating rate of 9 °C/min at a temperature of 600 °C in order to remove the micellar template. These samples were labelled ZMFO, ZMFO@CSO, ZMFO@F5-CSO, and ZMFO@F10-CSO, which are related to $Zn_{0.4}Mn_{0.6}Fe_2O_4$ core, $Zn_{0.4}Mn_{0.6}Fe_2O_4$@$CaSiO_3$, $Zn_{0.4}Mn_{0.6}Fe_2O_4$@Fe5-$CaSiO_3$, and $Zn_{0.4}Mn_{0.6}Fe_2O_4$@Fe10-$CaSiO_3$, respectively. The schematic illustration of synthesis of ZMFO and ZMFO@F-CSO nanocomposite is shown in Schem. 2.

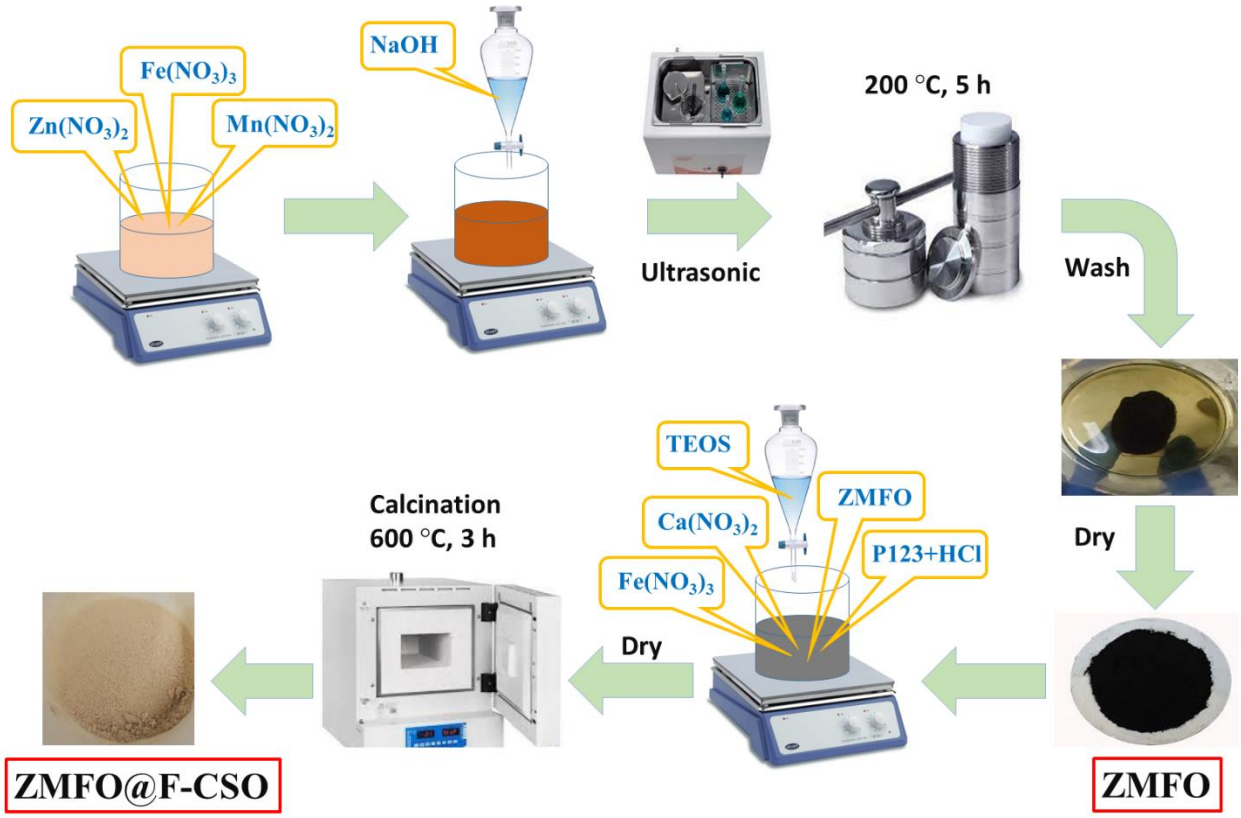


Schem. 2. The schematic illustration of synthesis of ZMFO and ZMFO@F-CSO.

**Measurement and characterization:**

Transmission electron microscopy (TEM, CM120, Netherlands) at an accelerating voltage of 100 kV and field emission scanning electron microscopy (FESEM, TESCAN, MIRA II, Czech Republic) were both used to study the morphological characterizations. The FESEM system carried out electron dispersion spectroscopy (EDS). Fourier transform infrared spectroscopy (FTIR) was recorded using a FTIR-AVATAR (Thermo, USA) with KBr pellets at room temperature over a frequency range of 4000–400 $cm^{-1}$. X-ray powder diffraction (XRD) data were collected using a copper K radiation source (l = 0.15405 nm, Philips, PW1730, Netherlands). The porous structural properties of the sample were analyzed by nitrogen adsorption-desorption isotherms at 77 K using the Belsorp Mini II, Japan. To perform the $N_2$ measurements, the samples were previously heated under vacuum for 120 min at 180 ˚C. The pore size distribution of the samples was calculated by Barrett–Joyner–Halenda (BJH) method from adsorption branch of the

isotherms. The magnetic properties of samples were measured by a VSM system with a maximum magnetic field of 15 kOe.

5 mg of synthetic nanoparticles were mixed with 5 mg of epirubicin in a water environment and stirred for 48 h. Then the mixture was centrifuged at 14000 rpm for 10 min, and the amount of unloaded epirubicin in the supernatant was determined through fluorometry (excitation at 488 nm and emission at 555 nm). Drug loading efficiency (Table 1) in the synthesized nanoparticles was evaluated indirectly according to the following equation:

$$Drug\ loading\ efficiency\ (\%) = \frac{loaded\ drug}{total\ drug\ amount} * 100$$

**Release test:**

2 mg drug-loaded nanoparticles were dispersed in 10 mL PBS (pH 7.4) and acetate buffer (pH 5.5) separately and shaken on a rotator for 120 h. 2, 4, 8, 12, 24, 48, 72, and 120 h later, a 0.5 mL sample was removed and replaced with fresh buffer. The drug concentration in samples was evaluated through fluorescence (excitation at 488 nm and emission at 555 nm). Released drug percent was evaluated according to the following equation:

$$Released\ drug\ percent = \frac{(Xn * Total\ buffer\ volume) + Xn - 1}{Total\ amount\ of\ drug} * 100.$$

where $X_n$ was drug amount determined in 1 mL buffer solution.

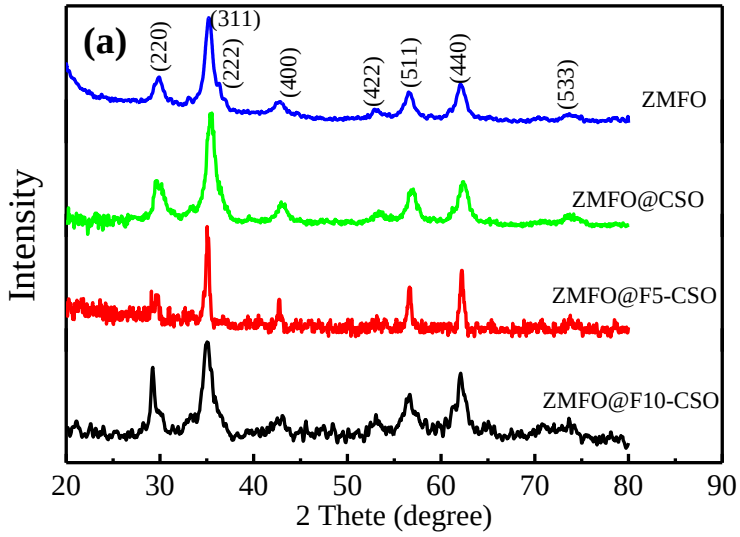


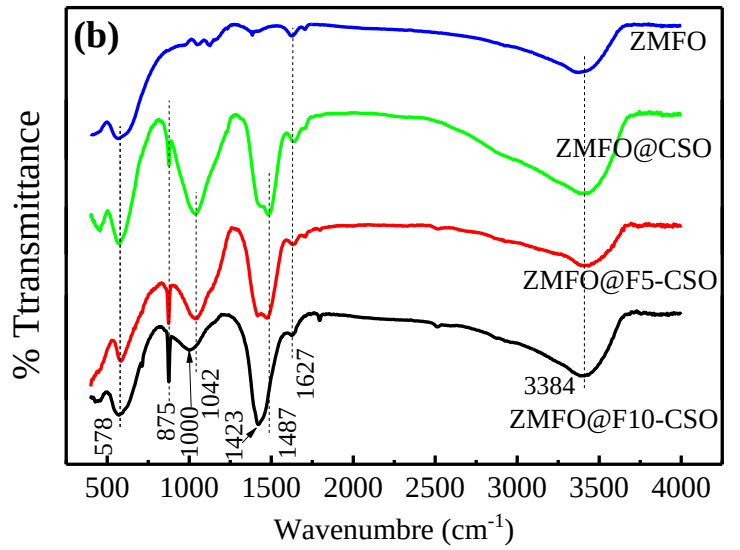


Fig. 1. (a) The XRD patterns, and (b) FTIR spectra of ZMFO, ZMFO@CSO, ZMFO@F5-CSO, and ZMFO@F10-CSO samples.

## 3- Results and discussion:

The XRD pattern is used to study the crystal structure properties of the samples, as illustrated in Fig. 1a. As can be seen in Fig. 1a, the characteristic diffraction peaks at $2\theta$ = 29.93°, 35.40°, 36.38°, 42.73°, 52.46°, 56.59°, 61.98°, and 74.95° of $ZnMnFe_2O_4$ correspond to the (220), (311), (222), (400), (422), (511), (440), and (533) planes of a cubic spinel structure with high crystallinity

(according to JCPDS No. 96-152-8318) (according to JCPDS No. The XRD patterns of the core-sell samples (ZMFO@F-CSO) show the coating of WS has not changed the core structure. Moreover, the structure of mesoporous $CaSiO_3$ has not changed after doping with Fe, indicating the substitution of iron ions instead of calcium [29].

The FTIR spectra of samples have been shown in Fig. 1b. As can be seen in Fig. 1b, the broad absorption peaks at 3384 and 1627 $cm^{-1}$ can be attributed to stretching and bending vibrations of OH on adsorbed water and the surfaces of samples, respectively [31, 32]. $ZnMnFe_2O_4$ microspheres exhibit typical bands at 578 $cm^{-1}$, which are attributed to Fe-O vibrations from the magnetite phase [33]. The bands at approximately 3384, 1627, and 578 $cm^{-1}$ are the same main infrared absorption peaks between ZMFO and various ZMFO@CSO. The peaks at 1487, 1042, and 857 $cm^{-1}$ belong to amorphous $CaSiO_3$ and can be attributed to asymmetric and symmetric stretching and bending vibrations of Si-O-Si, respectively [33]. These peaks in the ZMFO@F10-CSO spectrum have shifted to 1423 and 1000 $cm^{-1}$, due to the addition of more Fe. Thus, FTIR measurements confirm the formation of the samples.

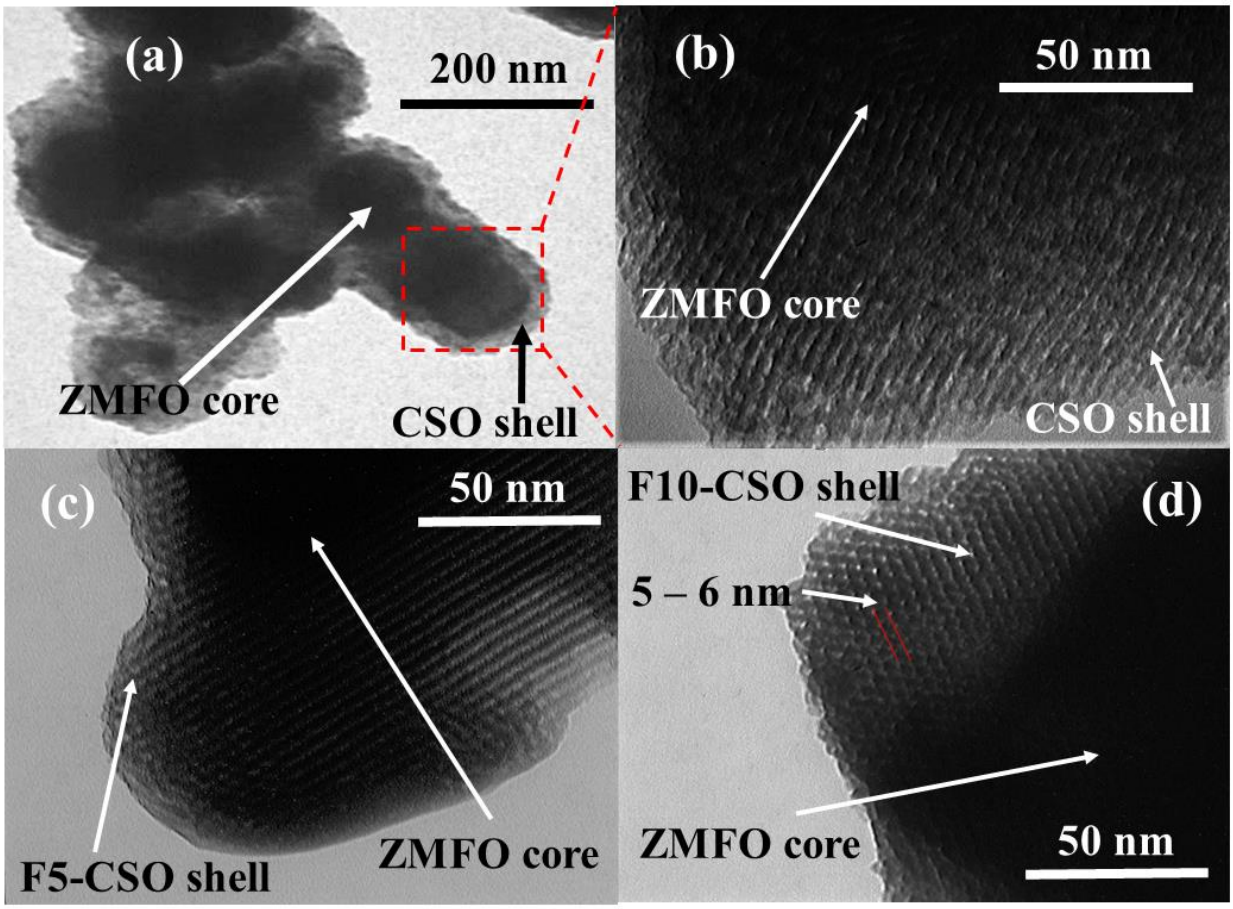


Fig. 2. The TEM images of (a) ZMFO@CSO core-shell nanoparticles, and (b) its magnified, (c) ZMFO@F5-CSO, and (d) ZMFO@F10-CSO nanocomposites.

The TEM images of the ZMFO@CSO nanoparticle core-shell samples are shown in Fig. 2. As can be seen in Fig. 2a, the synthesized particles are spherical-shaped and about 100–150 nm in size with a relatively suitable size distribution (the size distribution of nanoparticles is shown in Fig. 1S in Supporting Information). The TEM images of the ZMFO@CSO, ZMFO@F5-CSO, and ZMFO@F10-CSO core-shells have been shown in Figs. 2b–d as magnified, respectively. As can be observed in Figs. 2a-d, a spherical shell has covered the core homogeneously with a thickness of about 30-50 nm. In addition, the holes and porous surface of the shell can be observed from TEM images of the core-shell samples, which makes them suitable for use in medical applications [29]. The pore size of about 5–6 nm can be observed in all three samples of ZMFO@CSO,

ZMFO@F5-CSO, and ZMFO@F10-CSO, indicating the mesoporous structure of CaSiO3 has not been collapsed by doping with Fe.

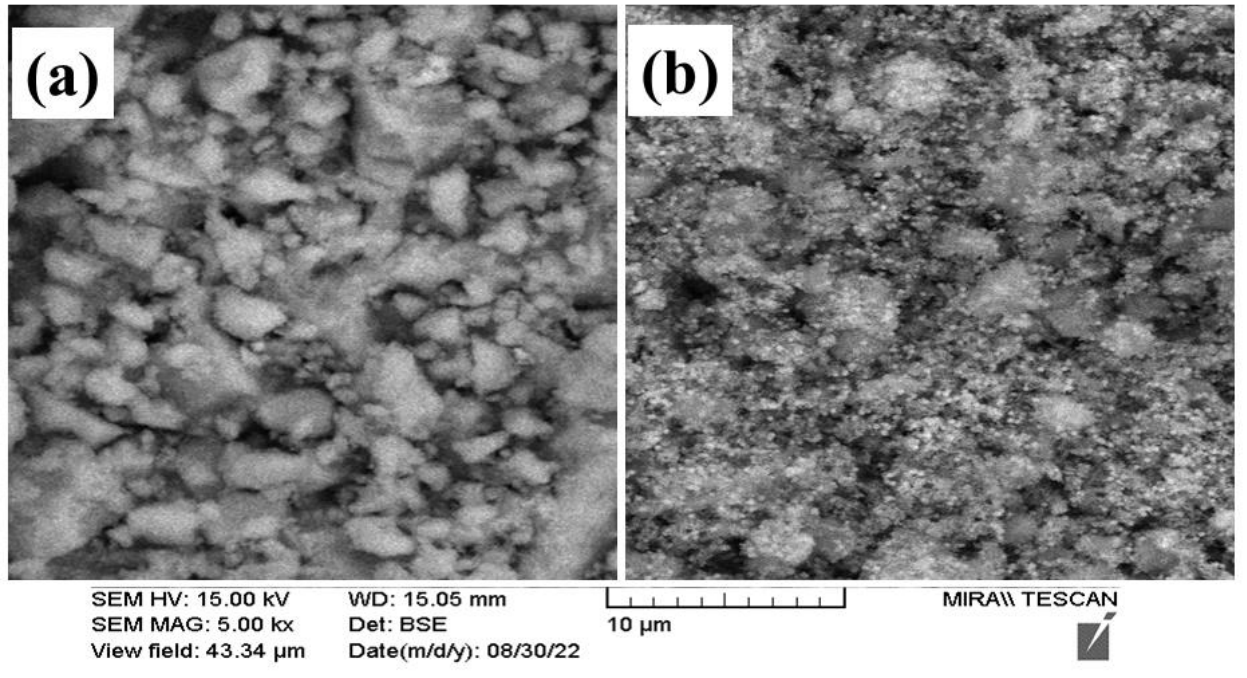


Fig. 3. The SEM images of (a) ZMFO nanoparticles, and (b) ZMFO@F5-CSO nanocomposites.

The surface morphologies of ZMFO nanoparticles and ZMFO@F5-CSO nanocomposites were characterized via SEM, as shown in Fig. 3a and b, respectively. As clearly shown in Fig. 3a, the ZMFO nanoparticles are relatively uniform, and rough. Light shade colors in Fig. 3b represent shell in ZMFO@F5-CSO and confirm core–shell structure.

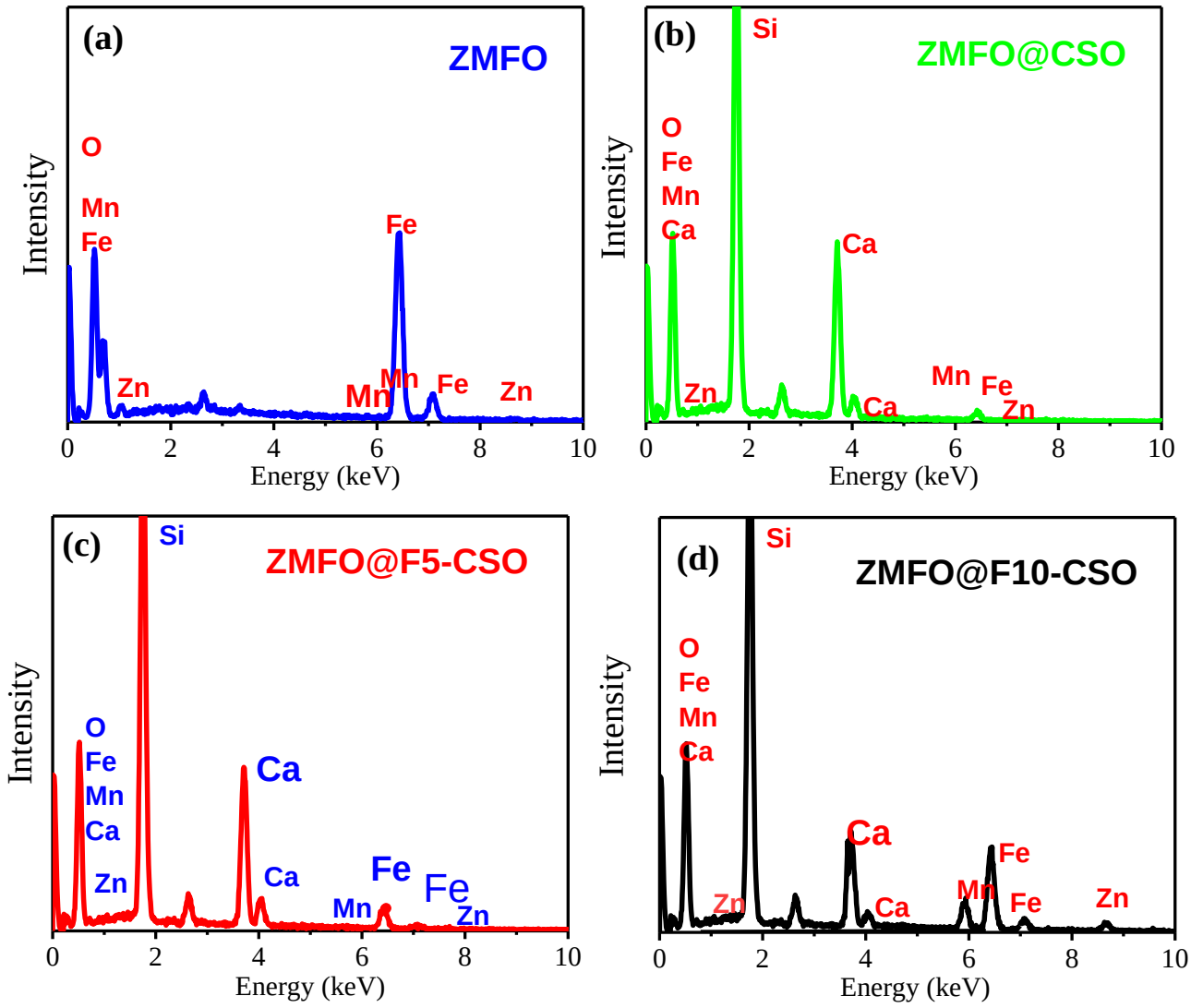


Fig. 4. The results of EDS analysis of (a) ZMFO nanoparticles, (b) ZMFO@CSO, (c) ZMFO@F5-CSO, and (d) ZMFO@F10-CSO nanocomposites.

The results of the EDS analysis of the samples are shown in Fig. 4. As can be seen in Fig. 4a, the elements Fe, Zn, Mn, and O are observed in the ZMFO sample. Also, the elements Fe, Zn, Mn, O, Ca, and Si can be seen in ZMFO@CSO, ZMFO@F5-CSO, and ZMFO@F10-CSO nanocomposite (Figs. 3b-d, respectively). Figs. 4a and 4b exhibit that the intensity of the Fe peak decreases in ZMFO@CSO, which can be attributed to coated CaSiO3 on ZMFO nanoparticles. But, in Figs. 4c and d, as expected, the intensity of the Fe peak increases in ZMFO@F5-CSO and ZMFO@F10-CSO. Here it should be noted that in the EDS analysis, most of the received signals

are coming from the surface of the sample as EDS detector was used in the scanning electron microscopy.

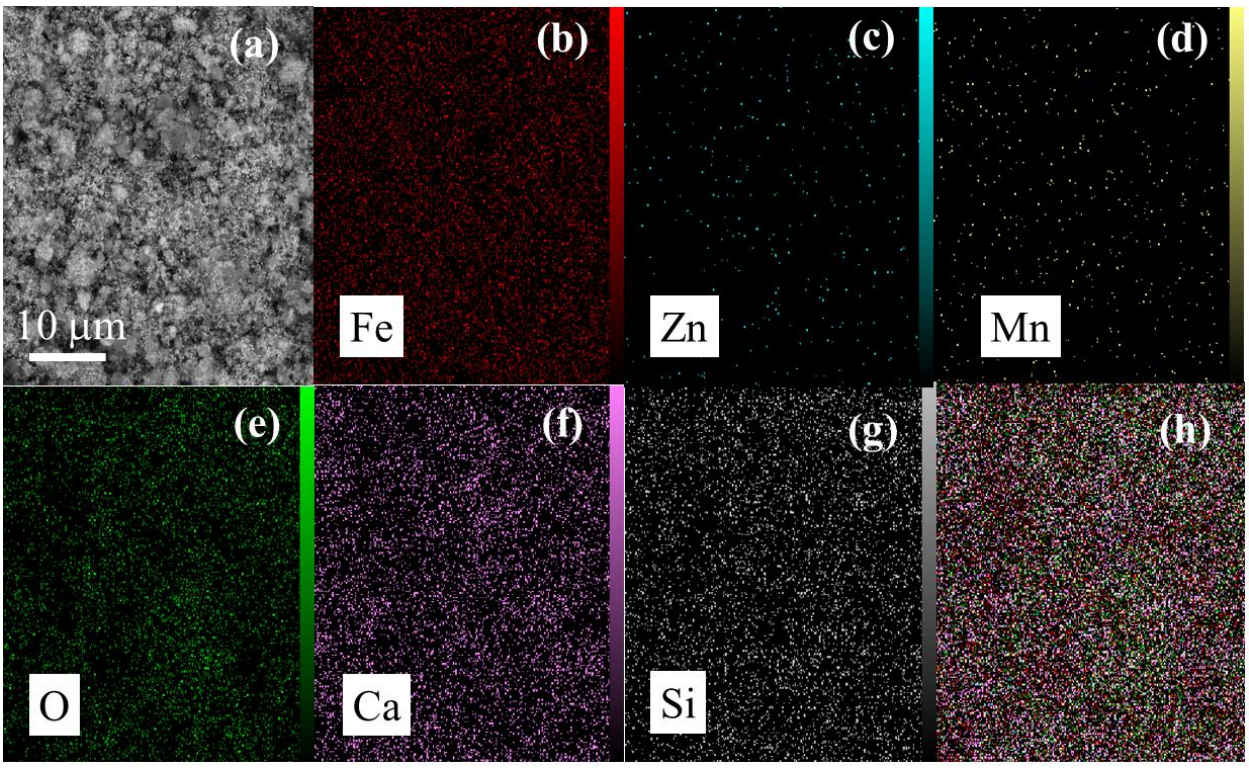


Fig. 5. (a) The SEM image of ZMFO@F10-CSO nanocomposite, and the elemental mapping of (b) Fe, (c) Zn, (d) Mn, (e) O, (f) Ca, (g) Si, and (h) all the elements.

The elemental mapping evaluates the uniform distribution of elements on the surface of the samples. The distribution of elements on the ZMFO@F10-CSO nanocomposite is shown in Fig. 5. Fig. 5a shows the SEM image of the ZMFO@F10-CSO nanocomposite, and Figs. 5b-g illustrate the distribution of Fe, Zn, Mn, O, Ca, and Si elements, respectively. As can be seen, the elements have an excellent uniform distribution on the surface. Also, Fig. 5h shows all the elements.

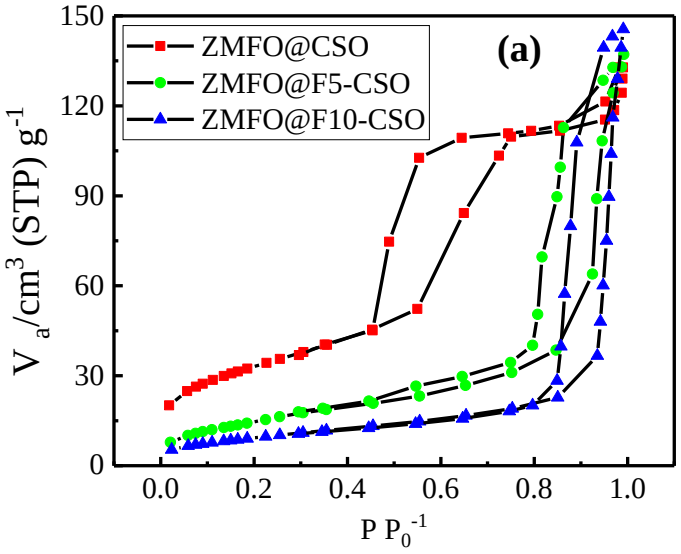


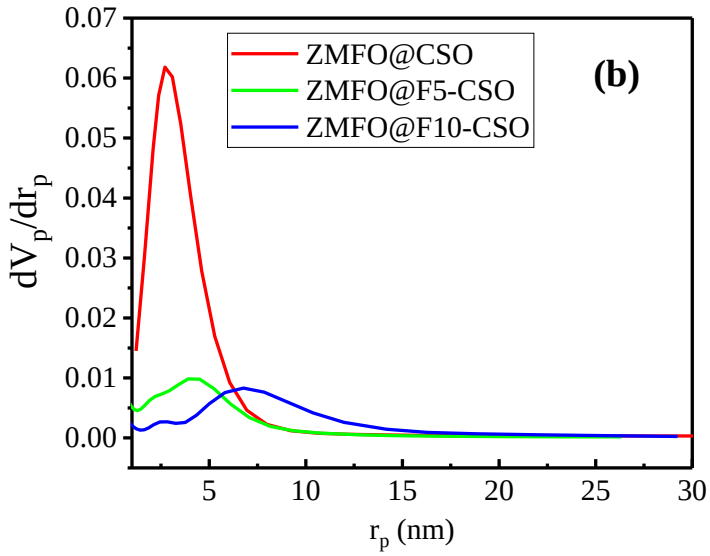


Fig. 6. The $N_2$ adsorption-desorption isotherms (a) and pore size distributions (b) of the samples.

The $N_2$ adsorption-desorption isotherms and their pore size distributions for ZMFO@CSO, ZMFO@F5-CSO, and ZMFO@F10-CSO have been shown in Fig. 6a and b. The BET surface area, total pore volume, and BJH pore size of the samples have been represented in Table 1. As can be seen from the isotherm curves in Fig. 6a, all the isotherms can be classified as type-IV

isotherms, indicating a well-ordered mesoporous structure [34-39]. The sample of ZMFO@CSO has an H2-type hysteresis loop in the mesoporous region [40]. On the other hand, by substituting Fe ions into the structure, the type hysteresis loop of the samples (ZMFO@F5-CSO and ZMFO@F10-CSO in Fig. 6a) has been gradually changed to an H1 type hysteresis loop [41]. Therefore, the inkbottle-like pores with narrow necks and variable size have been changed to cylindrical pores with both sides completely open by substitution of Fe ions in the structure. This change in pore shape can be obviously confirmed by comparison of TEM images of ZMFO@CSO and ZMFO@F5-CSO samples (Fig. 2b and 2c, respectively) which in both cases the TEM micrograph was taken perpendicular to lateral surface of the pores. The mentioned pore-shape changes can be due to accumulation of FeO molecules along the pore mouth that resulted in changing of the hysteresis loop from the H2 type to H1 by increasing the Fe substitution. In addition, it can result in enlargement of the pore width that is confirmed by the measurements of BJH pore size as presented in Table 1 and Fig. 6b. The pore size was clearly increased by increasing the Fe substitution. It could also be noted that the increase in the pore size and change in the hysteresis loops i.e. pore shape can be due to the larger Fe ion size than Ca ion size, resulting a greater metal oxygen bond length. Similar results were reported in the literatures when other types of transition element ions were incorporated in a silica framework [29, 42, 43]. Besides, increasing the Fe substitution in the structure decreases the BET surface area. The BET surface areas of 118.750, 55.196, and 34.543 $m^2/g$ were obtained for ZMFO@CSO, ZMFO@F5-CSO, and ZMFO@F10-CSO, respectively.

However, there is no doubt that these differences cannot cause a major change in the mesoporous scale when the Fe ions are accurately substituted into the $CaSiO_3$ structure as was revealed by former mentioned analyses. Thus, the mesoporous structure of $CaSiO_3$ was not destroyed after Fe substitution. At P $P_0^{-1}$ = 0.99, the ZMFO@CSO, ZMFO@F5-CSO, and ZMFO@F10-CSO samples had single-point adsorption with total pore volumes of 0.2043, 0.2096, and 0.2234 $cm^3/g$, respectively. Therefore, total pore volume is gradually raised with the increase of the Fe substitution, which can be due to the increasing of the attributed BJH pore size as described in Table 1. The results of the sample $N_2$ adsorption-desorption analysis show successful synthesis of mesoporous calcium silicate nanoparticles. Although the substitution of Fe decreases their surface area, the mesoporous structure of ZMFO@F10-CSO core-shell nanoparticles with

their large surface area of 34.543 $m^2/g$ should be a good candidate as a drug carrier in drug delivery systems.

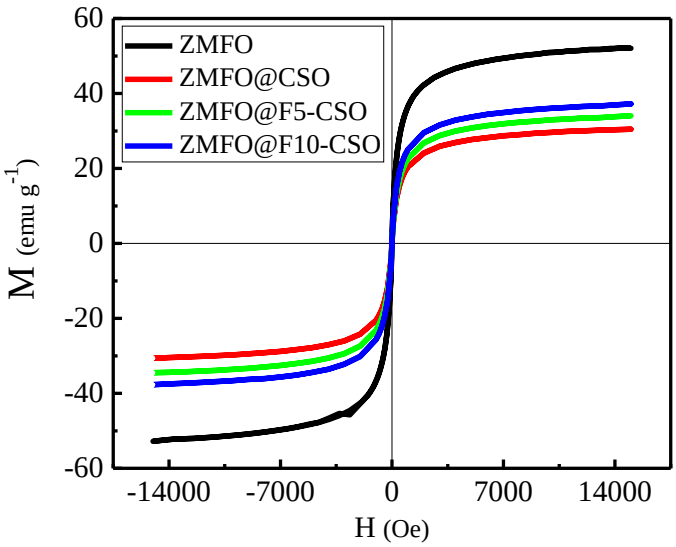


Fig. 7. The magnetization curves of all the samples.

The magnetic properties of the samples have been shown in Fig. 7. The magnetization curves of all the samples illustrate superparamagnetic behavior at room temperature. The magnetization saturation ($M_S$) of 52.09, 30.41, 34.05, and 37.22 emu/g were obtained for ZMFO, ZMFO@CSO, ZMFO@F5-CSO, and ZMFO@F10-CSO superparamagnetic nanoparticles, respectively. As can be seen, the measured $M_S$ of the ZMFO@CSO core-sell magnetic nanocomposite is less than that of the ZMFO nanoparticles by 21.07 emu/g, which can be attributed to the $CaSiO_3$ deposited on the surfaces of the ZMFO microspheres [33]. Despite this, $M_S$ increases with substitution of Fe in the mesoporous $CaSiO_3$ shell, which leads to a $M_S$ of 37.22 emu/g for ZMFO@F10-CSO at room temperature. The coercive magnetic field ($H_C$) of the samples was nearly 1 Oe, which is approximately constant for all the samples. Thus, the core-shell nanoparticles have been obtained, which, in addition to the mesoporous surface, show superparamagnetic behavior with a high $M_S$ of 37.22 emu/g and a low $H_C$ of 1 Oe (for the ZMFO@F10-CSO nanoparticle). These excellent properties make these nanoparticles capable of being used in medicine applications such as bone

regeneration [33, 44], magnetic hyperthermia [30], the EPI drug as a cancer drug [45], and MRI [46], due to their fast responses to external magnetic fields.

**Loading and release of drug:**

The drug was loaded into the mesoporous calcium silica superparamagnetic nanoparticles after incubation with EPI solution. At room temperature and under physiologic pH, the driving force for drug loading is the electrostatic interaction between negatively charged mesoporous calcium silica superparamagnetic nanoparticles (ZMFO@CSO, ZMFO@F5-CSO, and ZMFO@F10-CSO nanoparticles) and positively charged EPI. Approximately 98, 96, and 93% of the feeding drug were loaded into different nanoparticulate formulations. It can be attributed to an increase in pore size. Additionally, the ability of surfaces with more negative charges to more effectively adsorb positively charged EPI could account for this result. The release profile of EPI from the nanoparticles was assessed in buffer solutions at pH values of 5.5 and 7.2 to mimic the pH of tumors and normal tissues, respectively (Fig. 8). During the first two-hour period, at a pH of 5.5, about 49%, 32%, and 29% of the drug was released from the ZMFO@CSO, ZMFO@F5-CSO, and ZMFO@F10-CSO nanoparticles, respectively, while it was about 5%, 3%, and 2% at a pH of 7.4 for them in the phosphate buffer. This occurrence may be due to the fact that the zeta potential of ZMFO@CSO, ZMFO@F5-CSO, and ZMFO@F10-CSO nanoparticles depends on pH. On the other hand, in an acidic pH environment, protonation of surface sialon groups may cause drug epirubicin molecules to release from surface mesoporous calcium silica superparamagnetic, weakening their interaction with positively charged EPI and resulting in drug release. After 120 h, the drug release of 86%, 55%, and 54% was obtained for ZMFO@CSO, ZMFO@F5-CSO, and ZMFO@F10-CSO nanoparticles at pH 5.5 and 31%, 23%, and 20% for them at pH 7.4. As can be observed in Fig. 8, the drug release behavior of all the materials is the same. As a result, a drug nano carrier with pH-controlled release that hasn't had its surface altered has been created. Fig. 8 also shows that the drug is released continuously at the desired rate, which may be caused by the presence of mesoporous cells. They created a sequestered volume so that either the drug could be loaded as a single molecule into the mesoporous or the interaction between the drug and the nanoparticles in this constrained volume could be stronger. It would thus prevent an excessively rapid initial release [47]. Additionally, the drug release decreases with increasing

Fe percent in shell, which can be attributed to the fact that the different dissolution characteristics of the mesoporous ZMFO@F-CSO materials during drug release might play an important role in the different release rates from those materials. In similar reports, Zhang et al. [29] showed that the gentamicin release rate decreased with increasing Fe substitution in Fe–$CaSiO_3$ materials. Moreover, the gentamicin release rate decreased with increasing Sr substitution in Sr–$CaSiO_3$ materials [48], and this behavior was also reported by Wu et al. for dexamethasone release from bioactive SrO–$SiO_2$ glass [49]. Thus, the drug release rate can be to some extent controlled by the substitution of Fe for Ca in mesoporous F-CSO shell materials, and ZMFO@F-CSO core-shell nanocomposite has potential as a local drug delivery system.

Table 1. The surface area, total pore volume, and pore size of the samples

| **Samples** | **surface area ($m^2/g$)** | **Total pore volume ($cm^3/g$)** | **pore radius (nm)** | **Drug loading efficiency (%)** |
|---|---|---|---|---|
| **ZMFO@CSO** | 118.750 | 0.2043 | 2.38 | 93.52±0.3 |
| **ZMFO@F5-CSO** | 55.196 | 0.2096 | 3.97 | 95.67±0.45 |
| **ZMFO@F10-CSO** | 34.543 | 0.2234 | 6.20 | 98.39±0.04 |

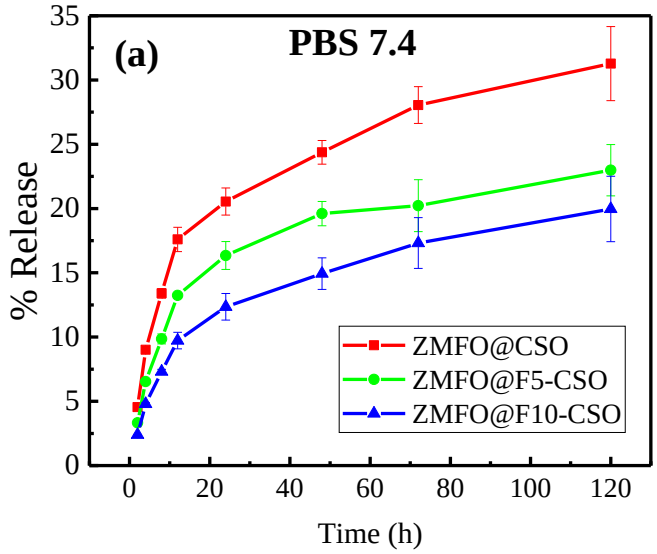


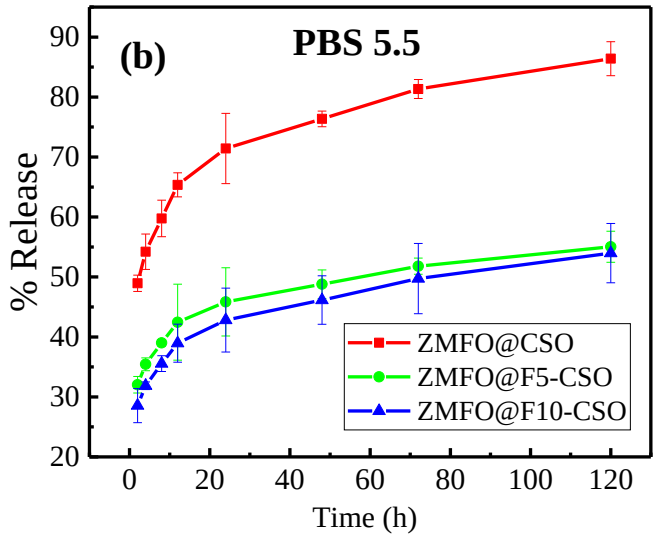


Figure 8. Drug release profile from PBS 7.4 (a) and acetate buffer 5.5 (b) during 120 h.

## Conclusion

In this work, we report the synthesis of a mesoporous iron-calcium silica superparamagnetic nanoparticle as $ZnMnFe_2O_4$@Fe-$CaSiO_3$ core-shell. The structural, morphological, magnetic, and

porosity analysis of the sample reveal a core-shell configuration with excellent properties such as mesoporous nanocomposite, superparamagnetic at room temperature, low toxicity, large surface area, tunable pore size, and easy surface manipulation. The $ZnMnFe_2O_4$ nanocomposite as a core is synthesized by the hydrothermal method, which shows superparamagnetic behavior with saturation magnetization of 52.09 emu/g. The core-shell structure is prepared by a surfactant-assisted sol-gel method to make pores on the surface of $CaSiO_3$. 10% doped Fe onto the calcium silica structure, i.e., $ZnMnFe_2O_4$@Fe10-$CaSiO_3$, shows a saturation magnetization and coercive magnetic field of 34.543 emu/g and 1 Oe, respectively. In addition, the core-shell mesoporous $ZnMnFe_2O_4$@Fe-$CaSiO_3$ nanocomposite reveals comparable mesoporous channels (3.4–6 nm), while the amorphous structure of $CaSiO_3$ does not change. The drug loading and release of these samples is evaluated by Epirubicin (EPI) as a model drug. It is found that an increase in iron ions improves the capacity to stabilize the pH environment. Also, these nanoparticles contained 98–93% of the feeding drug. Additionally, the mesoporous Fe-$CaSiO_3$ nanostructures demonstrate a sustained drug release property that could be applied in local drug delivery therapy. Therefore, these mesoporous superparamagnetic nanostructures would be a promising multifunctional platform with local drug delivery, magnetic resonance imaging, magnetic hyperthermia, and bone tissue regeneration.

## References

[1] P. Kumari, B. Ghosh, S. Biswas, Nanocarriers for cancer-targeted drug delivery, Journal of drug targeting, 24 (2016) 179-191.

[2] A.Y. Cai, Y.J. Zhu, C. Qi, Biodegradable inorganic nanostructured biomaterials for drug delivery, Advanced Materials Interfaces, 7 (2020) 2000819.

[3] Z. Chai, D. Ran, L. Lu, C. Zhan, H. Ruan, X. Hu, C. Xie, K. Jiang, J. Li, J. Zhou, Ligand-modified cell membrane enables the targeted delivery of drug nanocrystals to glioma, Acs Nano, 13 (2019) 5591-5601.

[4] N.H.M. Akhirudin, R. Shamsudin, N.K. Othman, The Effect of Different Concentrations of Calcium Silicate-Maghemite Coating towards Magnetic Behavior and Bioactivity, Sains Malaysiana, 49 (2020) 653-660.

[5] T.S. Stroup, N. Gray, Management of common adverse effects of antipsychotic medications, World Psychiatry, 17 (2018) 341-356.

[6] R. Porta, R. Borea, A. Coelho, S. Khan, A. Araújo, P. Reclusa, T. Franchina, N. Van Der Steen, P. Van Dam, J. Ferri, FGFR a promising druggable target in cancer: Molecular biology and new drugs, Critical reviews in oncology/hematology, 113 (2017) 256-267.

[7] B. Kang, M.-K. Shin, S. Han, I. Oh, E. Kim, J. Park, H.Y. Son, T. Kang, J. Jung, Y.-M. Huh, Magnetic nanochain-based smart drug delivery system with remote tunable drug release by a magnetic field, BioChip Journal, 16 (2022) 280-290.

[8] S.A. Shah, M.H. Asdi, M.U. Hashmi, M.F. Umar, S.-U. Awan, Thermo-responsive copolymer coated MnFe2O4 magnetic nanoparticles for hyperthermia therapy and controlled drug delivery, Materials Chemistry and Physics, 137 (2012) 365-371.

[9] P.G. Mazzola, A.M. Lopes, F.A. Hasmann, A.F. Jozala, T.C. Penna, P.O. Magalhaes, C.O. Rangel-Yagui, A. Pessoa Jr, Liquid–liquid extraction of biomolecules: an overview and update of the main techniques, Journal of Chemical Technology & Biotechnology: International Research in Process, Environmental & Clean Technology, 83 (2008) 143-157.

[10] M. Mabrouk, G.T. El-Bassyouni, H.H. Beherei, S.H. Kenawy, E.M. Hamzawy, Inorganic additives to augment the mechanical properties of 3D-printed systems, Advanced 3D-Printed Systems and Nanosystems for Drug Delivery and Tissue Engineering, Elsevier, 2020, pp. 83-107.

[11] J.C. Knight, P.G. Edwards, S.J. Paisey, Fluorinated contrast agents for magnetic resonance imaging; a review of recent developments, Rsc Advances, 1 (2011) 1415-1425.

[12] M. Wabler, W. Zhu, M. Hedayati, A. Attaluri, H. Zhou, J. Mihalic, A. Geyh, T.L. DeWeese, R. Ivkov, D. Artemov, Magnetic resonance imaging contrast of iron oxide nanoparticles developed for hyperthermia is dominated by iron content, International Journal of Hyperthermia, 30 (2014) 192-200.

[13] M.I.A.A. Maksoud, M.M. Ghobashy, A.S. Kodous, R.A. Fahim, A.I. Osman, H. Ala'a, D.W. Rooney, M.A. Mamdouh, N. Nady, A.H. Ashour, Insights on magnetic spinel ferrites for targeted drug delivery and hyperthermia applications, Nanotechnology Reviews, 11 (2022) 372-413.

[14] M.R. Abedin, S. Umapathi, H. Mahendrakar, T. Laemthong, H. Coleman, D. Muchangi, S. Santra, M. Nath, S. Barua, Polymer coated gold-ferric oxide superparamagnetic nanoparticles for theranostic applications, Journal of nanobiotechnology, 16 (2018) 1-13.

[15] R. Alwi, S. Telenkov, A. Mandelis, T. Leshuk, F. Gu, S. Oladepo, K. Michaelian, Silica-coated super paramagnetic iron oxide nanoparticles (SPION) as biocompatible contrast agent in biomedical photoacoustics, Biomedical optics express, 3 (2012) 2500-2509.

[16] B.-Q. Lu, Y.-J. Zhu, H.-Y. Ao, C. Qi, F. Chen, Synthesis and characterization of magnetic iron oxide/calcium silicate mesoporous nanocomposites as a promising vehicle for drug delivery, ACS applied materials & interfaces, 4 (2012) 6969-6974.
[17] S. Saravanan, S. Vimalraj, M. Vairamani, N. Selvamurugan, Role of mesoporous wollastonite (calcium silicate) in mesenchymal stem cell proliferation and osteoblast differentiation: a cellular and molecular study, Journal of Biomedical Nanotechnology, 11 (2015) 1124-1138.
[18] H.A. Aghdam, E. Sanatizadeh, M. Motififard, F. Aghadavoudi, S. Saber-Samandari, S. Esmaeili, E. Sheikhbahaei, M. Safari, A. Khandan, Effect of calcium silicate nanoparticle on surface feature of calcium phosphates hybrid bio-nanocomposite using for bone substitute application, Powder Technology, 361 (2020) 917-929.
[19] X. Guo, J. Wu, Y.-M. Yiu, Y. Hu, Y.-J. Zhu, T.-K. Sham, Drug–nanocarrier interaction—tracking the local structure of calcium silicate upon ibuprofen loading with X-ray absorption near edge structure (XANES), Physical Chemistry Chemical Physics, 15 (2013) 15033-15040.
[20] D. Zhao, J. Feng, Q. Huo, N. Melosh, G.H. Fredrickson, B.F. Chmelka, G.D. Stucky, Triblock copolymer syntheses of mesoporous silica with periodic 50 to 300 angstrom pores, science, 279 (1998) 548-552.
[21] W. Song, Z. Tang, D. Zhang, Y. Zhang, H. Yu, M. Li, S. Lv, H. Sun, M. Deng, X. Chen, Anti-tumor efficacy of c (RGDfK)-decorated polypeptide-based micelles co-loaded with docetaxel and cisplatin, Biomaterials, 35 (2014) 3005-3014.
[22] I.A. Hassanin, A.O. Elzoghby, Self-assembled non-covalent protein-drug nanoparticles: an emerging delivery platform for anti-cancer drugs, Expert Opinion on Drug Delivery, 17 (2020) 1437-1458.
[23] A. Charmforoushan, M.R. Roknabadi, N. Shahtahmassebi, B. Malaekeh-Nikouei, M. Bagherabadi, Synthesis and controlled drug release behavior of micro-mesoporous wollastonite nanoparticles. Effect of calcination temperature on the structural and biodegradability properties, Materials Chemistry and Physics, 280 (2022) 125825.
[24] W. Wan, H. Ouyang, W. Long, W. Yan, M. He, H. Huang, S. Yang, X. Zhang, Y. Feng, Y. Wei, Direct surface functionalization of cellulose nanocrystals with hyperbranched polymers through the anionic polymerization for ph-responsive intracellular drug delivery, ACS Sustainable Chemistry & Engineering, 7 (2019) 19202-19212.
[25] H. Miyajima, H. Touji, K. Iijima, Hydroxyapatite Particles from Simulated Body Fluids with Different pH and Their Effects on Mesenchymal Stem Cells, Nanomaterials (Basel), 11 (2021).

[26] B.Q. Jiang, S.F. Hu, Y.D. Liu, M.W. Wang, Polymerization of Silicone Modified Acrylate Emulsion and Preparation of Self-Cleaning Exterior Wall Paint, Advanced Materials Research, Trans Tech Publ, 2011, pp. 2055-2059.

[27] O. Cervantes, N. Casillas, P. Knauth, Z. Lopez, A. Virgen-Ortiz, O. Lozano, I. Delgado-Enciso, A. Sámano, S. Rosales, L. Martinez-Ceseña, An easily prepared ferrofluid with high power absorption density and low cytotoxicity for biomedical applications, Materials Chemistry and Physics, 245 (2020) 122752.

[28] K. Yamasaki, H. Hagiwara, Excess iron inhibits osteoblast metabolism, Toxicology letters, 191 (2009) 211-215.

[29] J. Zhang, Y. Zhu, J. Li, M. Zhu, C. Tao, N. Hanagata, Preparation and characterization of multifunctional magnetic mesoporous calcium silicate materials, Science and Technology of Advanced Materials, (2013).

[30] J. Yang, J. Zhang, C. Ding, D. Dong, P. Shang, Regulation of osteoblast differentiation and iron content in MC3T3-E1 cells by static magnetic field with different intensities, Biological trace element research, 184 (2018) 214-225.

[31] J. Wang, K. Zhang, Y. Zhu, Synthesis of SiO2-coated ZnMnFe2O4 nanospheres with improved magnetic properties, Journal of nanoscience and nanotechnology, 5 (2005) 772-775.

[32] A. Charmforoushan, M.R. Roknabadi, N. Shahtahmassebi, B. Malaekeh-Nikouei, Low temperature facile synthesis of pseudowollastonite nanoparticles by the surfactant-assisted sol-gel method, Materials Chemistry and Physics, 243 (2020) 122629.

[33] L. Liu, J. Liu, L. Zhao, Z. Yang, C. Lv, J. Xue, A. Tang, Synthesis and characterization of magnetic Fe3O4@ CaSiO3 composites and evaluation of their adsorption characteristics for heavy metal ions, Environmental Science and Pollution Research, 26 (2019) 8721-8736.

[34] K.S. Sing, Reporting physisorption data for gas/solid systems with special reference to the determination of surface area and porosity (Recommendations 1984), Pure and applied chemistry, 57 (1985) 603-619.

[35] R. Bafkary, S. Ahmadi, F. Fayazi, M. Karimi, Y. Fatahi, S.M. Ebrahimi, F. Atyabi, R. Dinarvand, Amphiphilic hyperbranched polyester coated rod mesoporous silica nanoparticles for pH-responsive doxorubicin delivery, DARU Journal of Pharmaceutical Sciences, 28 (2020) 171-180.

[36] W. Xia, J. Chang, Preparation and the phase transformation behavior of amorphous mesoporous calcium silicate, Microporous and mesoporous materials, 108 (2008) 345-351.

[37] S. Chen, R. Wang, Surface area, pore size distribution and microstructure of vacuum getter, Vacuum, 85 (2011) 909-914.

[38] S. Shariati, M. Khabazipour, F. Safa, Synthesis and application of amine functionalized silica mesoporous magnetite nanoparticles for removal of chromium (VI) from aqueous solutions, Journal of Porous Materials, 24 (2017) 129-139.
[39] S. Lowell, J.E. Shields, M.A. Thomas, M. Thommes, Characterization of porous solids and powders: surface area, pore size and density, Springer Science & Business Media, 2006.
[40] L. Ernawati, R.A. Wahyuono, A.D. Laksono, A. Ningrum, K. Handayani, A. Sabrina, Wollastonite (CaSiO3)-Based Composite Particles for Synthetic Food Dyes (Brilliant Blue) Removal in Aquatic Media: Synthesis, Characterization and Kinetic Study, IOP Conference Series: Materials Science and Engineering, IOP Publishing, 2021, pp. 012001.
[41] M. Vallet-Regí, C.V. Ragel, A.J. Salinas, Glasses with medical applications, European Journal of Inorganic Chemistry, 2003 (2003) 1029-1042.
[42] G. Du, S. Lim, Y. Yang, C. Wang, L. Pfefferle, G.L. Haller, Catalytic performance of vanadium incorporated MCM-41 catalysts for the partial oxidation of methane to formaldehyde, Applied Catalysis A: General, 302 (2006) 48-61.
[43] N.W.C. Jusoh, A.A. Jalil, S. Triwahyono, H.D. Setiabudi, N. Sapawe, M.A.H. Satar, A.H. Karim, N.H.N. Kamarudin, R. Jusoh, N.F. Jaafar, N. Salamun, J. Efendi, Sequential desilication–isomorphous substitution route to prepare mesostructured silica nanoparticles loaded with ZnO and their photocatalytic activity, Applied Catalysis A: General, 468 (2013) 276-287.
[44] L. Ansari, M.R. Jaafari, T.R. Bastami, B. Malaekeh-Nikouei, Improved anticancer efficacy of epirubicin by magnetic mesoporous silica nanoparticles: in vitro and in vivo studies, Artificial Cells, Nanomedicine, and Biotechnology, 46 (2018) 594-606.
[45] M.Y. Hanafi-Bojd, S.A. Moosavian Kalat, S.M. Taghdisi, L. Ansari, K. Abnous, B. Malaekeh-Nikouei, MUC1 aptamer-conjugated mesoporous silica nanoparticles effectively target breast cancer cells, Drug development and industrial pharmacy, 44 (2018) 13-18.
[46] S.y. Guo, D. Sun, D.l. Ni, M.r. Yu, K. Qian, W. Zhang, Y.w. Yang, S. Song, Y. Li, Z.y. Xi, Smart tumor microenvironment-responsive Nanotheranostic agent for effective cancer therapy, Advanced Functional Materials, 30 (2020) 2000486.
[47] J.M.R. Ansari L., Rohani Bastami T., Malaekeh-Nikouei B., Improved anticancer efficacy of epirubicin by magnetic mesoporous silica nanoparticles: in vitro and in vivo studies, Artificial Cells, Nanomedicine, and Biotechnology, 46 (2018) 594-606.
[48] Y. Zhu, M. Zhu, X. He, J. Zhang, C. Tao, Substitutions of strontium in mesoporous calcium silicate and their physicochemical and biological properties, Acta Biomaterialia, 9 (2013) 6723-6731.

[49] C. Wu, W. Fan, M. Gelinsky, Y. Xiao, P. Simon, R. Schulze, T. Doert, Y. Luo, G. Cuniberti, Bioactive SrO–SiO2 glass with well-ordered mesopores: Characterization, physiochemistry and biological properties, Acta Biomaterialia, 7 (2011) 1797-1806.

- Synthesis of a mesoporous calcium silicate superparamagnetic as $ZnMnFe_2O_4$@Fe-$CaSiO_3$
- $ZnMnFe_2O_4$@Fe-$CaSiO_3$ reveals mesoporous channels with amorphous structure of $CaSiO_3$
- $M_s$ and $H_c$ of $ZnMnFe_2O_4$@Fe10-$CaSiO_3$ are 34.543 emu/g and 1Oe
- Increase of iron ions improved the capacity to stabilize the pH environment
- $ZnMnFe_2O_4$@Fe10-$CaSiO_3$ nanoparticles are contained 98 - 93% of the feeding drug

AUTHOR DECLARATION

We wish to confirm that there are no known conflicts of interest associated with this publication and there has been no significant financial support for this work that could have influenced its outcome.
We confirm that the manuscript has been read and approved by all named authors and that there are no other persons who satisfied the criteria for authorship but are not listed. We further confirm that the order of authors listed in the manuscript has been approved by all of us.
We confirm that we have given due consideration to the protection of intellectual property associated with this work and that there are no impediments to publication, including the timing of publication, with respect to intellectual property. In so doing we confirm that we have followed the regulations of our institutions concerning intellectual property.
We understand that the Corresponding Author is the sole contact for the Editorial process (including Editorial Manager and direct communications with the office). He/she is responsible for communicating with the other authors about progress, submissions of revisions and final approval of proofs. We confirm that we have provided a current, correct email address which is accessible by the Corresponding Author.

Authors:

**Aqeel Al-Hamaidah,**

**Mahmood Rezaee Roknabadi,**

**Malek Bagheri Harouni,**

**Bizhan Malaekeh-Nikouei,**

**Asma Mahmoudi,**

**Reza Ghanbari,**

**Alireza Charmforoushan**

Sincerely yours,
Malek Bagheri Harouni
E-mail: